THE JOURNAL OF PHYSICAL CHEMISTRY B
A JOURNAL OF THE AMERICAN CHEMICAL SOCIETY

pubs.acs.org/JPCB

Article

Coarse-Grained Simulations of DNA Reveal Angular Dependence of Sticky-End Binding

Published as part of The Journal of Physical Chemistry virtual special issue "Ruth Nussinov Festschrift".

Nicholas M. Gravina, James C. Gumbart, and Harold D. Kim*

Cite This: *J. Phys. Chem. B* 2021, 125, 4016–4024

Read Online

ACCESS | Metrics & More | Article Recommendations | Supporting Information

ABSTRACT: Annealing between sticky ends of DNA is an intermediate step in ligation. It can also be utilized to program specific binding sites for DNA tile and origami assembly. This reaction is generally understood as a bimolecular reaction dictated by the local concentration of the sticky ends. Its dependence on the relative orientation between the sticky ends, however, is less understood. Here we report on the interactions between DNA sticky ends using the coarse-grained oxDNA model; specifically, we consider how the orientational alignment of the double-stranded DNA (dsDNA) segments affects the time required for the sticky ends to bind, τ_b. We specify the orientation of the dsDNA segments with three parameters: θ, which measures the angle between the helical axes, and ϕ_1 and ϕ_2, which measure rotations of each strand around the helical axis. We find that the binding time depends strongly on both θ and ϕ_2: ~20-fold change with θ and 10-fold change with ϕ_2. The binding time is the fastest when the helical axes of duplexes are pointing toward each other and the sticky ends protrude from the farthest two points. Our result is relevant for predicting hybridization efficiency of sticky ends that are rotationally restricted.

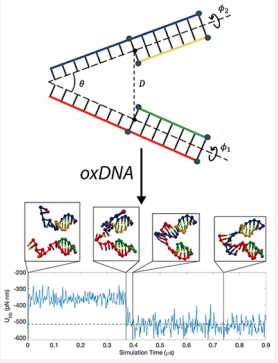

INTRODUCTION

Hybridization or annealing between sticky ends is commonly used as an intermediate step to ligation or assembly of DNA nanostructures. The sticky ends are two complementary single strands of DNA that extend from a DNA duplex. In a bimolecular reaction, the sticky ends undergo diffusive encounters at random relative orientations. Hence, the annealing rate would be an average over all relative orientations and depend solely on the local concentration of sticky ends. But in many cases such as in DNA cyclization[1,2] or in DNA origami platforms or building blocks,[3−6] the relative orientation of the sticky ends can be restricted. Inside the cell, DNA damage can cause a DNA double-strand break. In a repair pathway called alternative end joining,[7,8] sticky ends are generated at the broken ends for subsequent ligation. In this process, the sticky ends are held in close proximity and likely to be rotationally restricted as well. Consequently, the annealing rate between rotationally restricted sticky ends will depend on the orientation factor.[9] But how the relative orientation between the sticky ends influences their annealing efficiency is not clear.

In both biological and nanotechnological contexts, theoretical and computational models have been widely exploited to probe the behavior of DNA. Quantum chemistry calculations have been used to study the interactions between nucleotides in great detail.[10−12] However, the high computational cost of these methods limits their scope to the study of interactions between nearest-neighbor base pairs in a vacuum. Classical all-atom approaches, in which every atom of DNA and surrounding solvent is accounted for as a point particle governed by effective interactions, have been used extensively in the study of short DNA segments[13−17] and have recently been applied to larger DNA systems.[18,19] However, because these methods are limited to microsecond time scales, simulating processes such as the breaking and formation of base pairs (so-called "rare-event" processes) remain a challenge.[20] Theoretical approaches, such as the wormlike chain model,[21] have been developed to understand large-scale properties of DNA; however, these approaches are not detailed enough to address processes such as duplex formation.[20] Coarse-grained DNA models lie between the extremes of analytical and all-atom approaches: the approximations made by these models imply a compromise between computational efficiency and accuracy that allows for simulation of larger time scales.[20,22] In particular, coarse-grained DNA models have been used to analyze DNA hybridization,[23−25] the behavior of DNA under torsional[26] and tensile[27] stress, and DNA duplex melting.[28]

One of the most popular coarse-grained models is oxDNA2, which is an improved version of the original oxDNA model

Received: January 17, 2021
Revised: April 6, 2021
Published: April 19, 2021

Downloaded via GEORGIA INST OF TECHNOLOGY on August 2, 2021 at 06:00:34 (UTC).
See https://pubs.acs.org/sharingguidelines for options on how to legitimately share published articles.

ACS Publications

© 2021 American Chemical Society

https://doi.org/10.1021/acs.jpcb.1c00432
J. Phys. Chem. B 2021, 125, 4016–4024

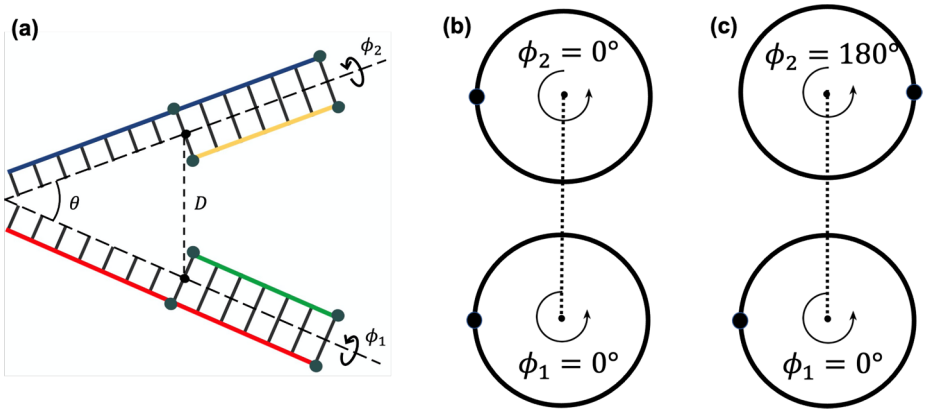

Figure 1. Parameters and strand configurations for the simulation. (a) Schematic showing the four parameters that define the orientation of the sticky ends. θ is the angle between the helical axes of the DNA segments. ϕ_1 and ϕ_2 specify counterclockwise rotations around the helical axis for segment 1 and 2, respectively. D is the distance between the midpoints of the final base pair on the sticky-end side of the DNA segments. In all trials, D remains fixed at 2.66 nm, a value obtained by using oxDNA to measure the length of a double helix identical in sequence to the sticky ends used in simulation. Each of the gray dots along the colored DNA backbones represents a point at which an external force was applied to restrain the motion of the DNA strand. These forces were all derived from harmonic potentials with equilibrium points at the initial location of the backbone site and the same spring constant. (b, c) Schematics showing example cis and trans configurations of the DNA segments. The views in each figure are presented along the helical axes, represented by the dots in the center of each circle, which represents the DNA helix. The large dots on the circle represent the juncture between the sticky ends and the dsDNA segments, i.e., the "attachment points". The dashed line down the center of each schematic represents the plane containing both helical axes, one from each strand. Both ϕ_1 and ϕ_2 are counterclockwise rotations about their respective helical axis. (b) Example of the cis configuration where both attachment points are on the same side of the plane containing the helical axes. (c) Example of the trans configuration where both attachment points are on opposite sides of the plane containing the helical axes.

created by Ouldridge et al. in 2011.[29] Both oxDNA and oxDNA2 were designed with a heuristic, "top-down" approach, focusing on reproducing well-known properties of DNA (such as the helical structure of the B-DNA duplex) and experimental results (such as duplex melting temperatures).[20] The oxDNA model treats each nucleotide as a rigid body with three interaction sites, each of which has mutual, highly anisotropic interactions. This coarse-grained approach is detailed enough to obtain good agreement with measurements of the structural, mechanical, and especially the thermodynamic properties of single-stranded DNA (ssDNA) and double-stranded DNA (dsDNA).[20,29] Consequently, the model has provided key insights into many different areas of research, including DNA nanotechnology,[30−33] DNA origami,[34,35] and DNA biophysics.[26,27,36−39] In this study, we thus employed the coarse-grained oxDNA2 model to investigate the orientation dependence of sticky-end annealing. We found a significant dependence between the orientation of the dsDNA segments and the binding rate of sticky ends, which reflects the finite bend and twist persistence lengths of ssDNA overhangs.

METHODS

For all simulations, we employed the same sequence to create our dsDNA segments and sticky ends. Each DNA segment was composed of a dsDNA segment of seven base pairs in length and a sticky end of seven nucleotides in length. The dsDNA segments were both composed of the sequence TCCCGAT (5′ to 3′) and its complementary sequence. The sticky end for strand 1 has sequence AATGTCC, and the sticky end for strand 2 has sequence GGACATT, both given here from 5′ to 3′. Although the oxDNA2 model is capable of accounting for sequence-dependent effects, we chose to forego this feature and used the hard-coded average parameters for base pairing and stacking interaction strengths.

To interrogate the relationship between the orientation of the sticky ends and the time required to reach the bound state, τ_b, we imposed restraints on the DNA strands to fix the values of the orientation variables (see Figure 1a). These restraints prevented the DNA strands from freely diffusing and thereby altering their relative orientation. We restrained four phosphate backbone particles on each dsDNA segment during the simulations: for the shorter ssDNA strand that did not contain the sticky end, we restrained the phosphate backbone particles at the 3′ and 5′ ends; for the longer ssDNA that contained the sticky end, we restrained the 5′ end phosphate backbone particle and the phosphate backbone particle forming the terminal base pair before the start of sticky end (see Figure 1a). We utilized the external force feature of oxDNA to apply harmonic potentials to each of these points, placing the equilibrium position at each particle's starting position. Each harmonic potential used a force constant of 57.09 pN/nm. The other particles comprising the DNA segments in oxDNA were free to move during the simulation. In addition to considering the effect of orientation on the time required for the sticky ends to bond in our simulations, we also considered its effect on the pathway of sticky-end binding, namely, the order in which base pairs formed between the annealing sticky ends. To do this, we assigned a number 0−6 to each sticky-end base pair and recorded the identity of the base pair(s) present in the first bound configuration (see Figure 5).

To initialize the simulation, we chose to select sticky-end configurations from previous runs and attach them to the initialized duplexes to form different sticky-end initial configurations (SEICs). The default initial condition for the sticky ends chosen by oxDNA is a single helix, in which the sticky end spirals out from the dsDNA segment as if it were bound to a complementary strand. In addition to being a thermodynamically unlikely configuration, this configuration results in steric clash when θ is close to 180°. The SEICs served to replace the improbable default initial configuration and to minimize steric clash by allowing the sticky ends to leave the plane containing the helical axes of the dsDNA

https://doi.org/10.1021/acs.jpcb.1c00432
J. Phys. Chem. B 2021, 125, 4016−4024

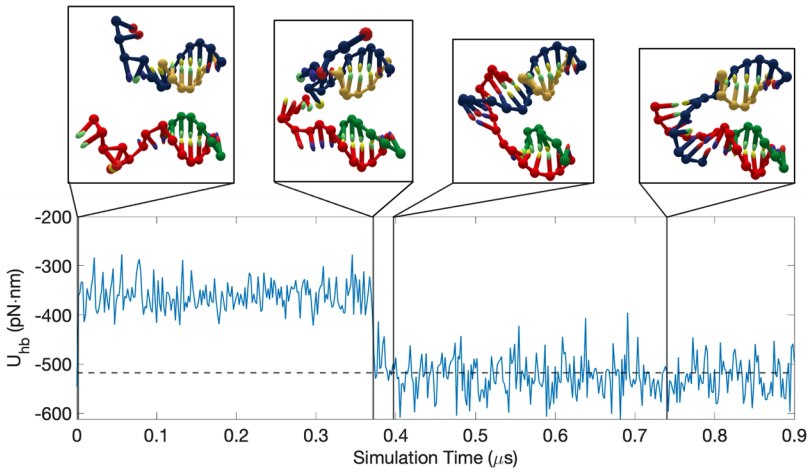

Figure 2. Hydrogen-bonding energy U_{hb} as a function of simulation time for the configuration $(\theta, \phi_1, \phi_2) = (0°, 180°, 0°)$ with SEIC 0. The horizontal line denotes the −517.79 pN·nm energy threshold that indicates full sticky-end binding. Conformations at select points along the trajectory show the initial configuration, the conformation immediately before annealing, and the conformation fully annealed. They are displayed above the hydrogen-bonding energy trajectory with vertical lines denoting the time at which each configuration was sampled. τ_b corresponds to the time interval between the first two configurations shown.

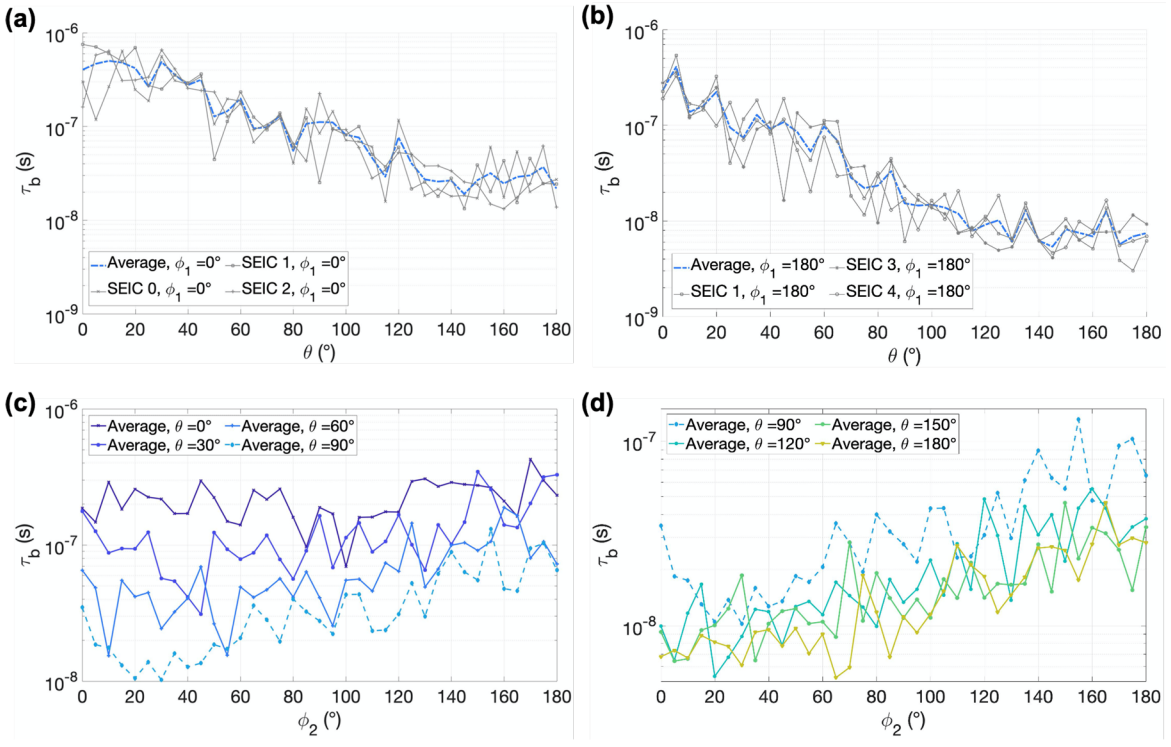

Figure 3. Dependence of the binding time on axial and azimuthal angles. (a) Time to bond τ_b as a function of θ with $\phi_1 = \phi_2 = 0°$. (b) Time to bond τ_b as a function of θ with $\phi_1 = 180°$ and $\phi_2 = 0°$. Each point on the plots represents an average τ_b: the dashed blue curves represent $\overline{\tau}_b$, the average across all the SEICs used with the corresponding ϕ_1; the gray points on each plot represent averages over four trials with an initial configuration specified by (θ, ϕ_1, ϕ_2) and an SEIC. Both plots show an exponential decrease in τ_b from an initial maximum at $\theta = 0°$ that ends around $\theta = 120°$. The general trend of decrease in τ_b as θ increases indicates that sticky-end binding occurs most rapidly when the dsDNA strands' helical axes are collinear. For the $\phi_1 = 180°$ case, all average τ_b values at a given θ are less than the average τ_b value at the same θ when $\phi_1 = 0°$. This indicates that binding occurs more rapidly in the trans configuration. (c) Average binding time $\overline{\tau}_b$ as a function of ϕ_2 for $\theta = 0°$, 30°, 60°, and 90°. (d) Average binding time $\overline{\tau}_b$ as a function of ϕ_2 for $\theta = 90°$, 120°, 150°, and 180°. Each point on the plots represents a $\overline{\tau}_b$, the average across all the SEICs used with the corresponding (θ, ϕ_1, ϕ_2). There are data from two SEICs for every ϕ_2. Because steric clashes limited the use of certain SEICs, some plots have data from three SEICs to ensure $\overline{\tau}_b$ is computed with two SEICs for every ϕ_2. For every data point presented, ϕ_1 is held constant at 180°. Data for $\theta = 90°$ (shown as dashed blue lines) are included in both plots to provide a sense of scale and clearly present the trend of decrease in $\overline{\tau}_b$ as θ increases. The standard deviation for these measurements is ≈20% of the corresponding $\overline{\tau}_b$.

segments. To conduct the first round of simulations, we selected a total of five SEICs (SEIC 0−4). Each of these SEICs was chosen from previous runs that used the same DNA strands. For the second round of simulations varying temperature, we sampled SEICs from a simulation with each sticky end exchanged for polyT segments. This yielded a

https://doi.org/10.1021/acs.jpcb.1c00432
J. Phys. Chem. B 2021, 125, 4016−4024

repository of 200 additional sticky-end configurations (205 total). To change the strand configuration, the sticky ends and the dsDNA segments were rotated as a unit to achieve the desired θ, ϕ_1, and ϕ_2 angles, i.e., the position of each nucleotide composing the sticky ends relative to the dsDNA segment remains constant. At a given angular configuration specified by (θ, ϕ_1, ϕ_2), certain SEICs resulted in steric clashes. For the first round of simulations, we selected at least two SEICs from SEICs 0−4 per configuration that contained no overlapping particles to conduct our simulations.

For the second round, we conducted simulations at three temperatures (283, 310, and 363 K) to determine how temperature affects the binding time and the free energy profile of sticky-end binding. At each of these temperatures we measured the average binding time τ_b using ∼20 SEICs for angular configurations given by (θ, ϕ_1, ϕ_2) = (120°, 180°, 20°), (θ, ϕ_1, ϕ_2) = (90°, 180°, 90°), and (θ, ϕ_1, ϕ_2) = (0°, 180°, 170°). These configurations were chosen because they correspond to low, medium, and high values for τ_b as determined by the first round of simulations. Hence, we will refer to them as the low τ_b, medium τ_b, and high τ_b configurations (see Figure 6). For each of the nine temperature and configuration pairs, we also calculated the free energy as a function of the number of sticky-end base pairs (see Figure 7). The free energies were computed by using biased virtual-move Monte Carlo (VMMC) simulations in combination with the dynamic histogram analysis method.[40,41] Every simulation was conducted with a salt concentration of 0.5 M and a D of 2.66 nm, a value obtained by using oxDNA to measure the length of a double helix identical in sequence to the sticky ends used in simulation (see Figure 1). During our simulations, we did not make any special considerations for transient states with mismatched base pairs.

RESULTS

For each initial configuration of the DNA strands specified by (θ, ϕ_1, ϕ_2) and an SEIC, we conducted four trials. In each trial, we recorded the time at which the hydrogen bonding energy first reached −517.79 pN·nm, i.e., the energy for full binding between all complementary sticky-end nucleotides. We present a typical time trajectory of hydrogen bonding energy in Figure 2. The four trials yielded the mean binding time τ_b, which we then averaged again across runs with different SEIC to obtain a $\overline{\tau}_b$ for a given θ, ϕ_1, and ϕ_2. These runs were completed in two groups: one varying θ from 0° to 180° in steps of 5° with ϕ_1 = 0° and 180° and another varying ϕ_2 from 0° to 180° in steps of 5° at various θ values. We employed a temperature of 310 K and a salt concentration of 0.5 M for these simulations. As θ represents the angle between the two helical axes, the helices point in the same direction at θ = 0° (parallel) and in opposite directions at θ = 180° (antiparallel). ϕ angles represent rotations around the helical axes; therefore, the sticky ends are on the same side of the helix when ϕ_1 = 0°, ϕ_2 = 0° (the "cis" configuration) and on opposite sides when ϕ_1 = 0°, ϕ_2 = 180° (the "trans" configuration). These two extreme configurations are presented in Figure 1. In general, $\Delta\phi \equiv |\phi_1 - \phi_2| < 180°$.

In Figure 3 we present τ_b as a function of θ, the angle between the two helical axes. Figure 3a shows τ_b as a function of θ with ϕ_1 = 0° for three different SEICs. Figure 3b shows τ_b as a function of θ with ϕ_1 = 180° for three different SEICs. We also present the average across these SEICs $\overline{\tau}_b$ (shown in blue). The standard deviation for these measurements is ≈20% of the corresponding $\overline{\tau}_b$. In these graphs, θ increases in steps of 5° from 0°, where the two dsDNA segments are parallel, to 180°, where the two dsDNA segments are antiparallel. In both cases (ϕ_1 = 0° and ϕ_1 = 180°), the binding time decreases as θ increases: sticky-end annealing is slowest when the helices are parallel and fastest when the helices are antiparallel. In addition to the θ dependence, ϕ_1 also modulates $\overline{\tau}_b$. By comparing Figures 3a and 3b, one can see that $\overline{\tau}_b$ with ϕ_1 = 180° is globally shorter than $\overline{\tau}_b$ with ϕ_1 = 0°, indicating a preference for the trans configuration as opposed to the cis configuration.

To further explore the relationship between τ_b and the ϕ angles, we measured τ_b when varying ϕ_2. In Figure 3, we present τ_b as a function of ϕ_2 at various θ with ϕ_1 = 180°. For θ = 0° there is little to no increase in τ_b as ϕ_2 increases from 0° to 180°. For all other θ, there is an increase in τ_b as ϕ_2 increases, indicating that bonding occurs more rapidly when the strands are closer to the trans configuration than the cis configuration. As shown in Figure 3, there is a decrease in $\overline{\tau}_b$ as θ increases; the $\overline{\tau}_b$ curve for a particular θ is typically less than the $\overline{\tau}_b$ curve for a smaller θ at any given ϕ_2.

In Figure 4, we present the effects of θ and ϕ on the binding time τ_b using a heatmap. The vertical axis represents θ while the horizontal axis represents ϕ_2. ϕ_1 is held constant at 180°. Within a given ϕ_2 value, the binding time τ_b decreases as θ increases in the same manner as shown in Figure 3, although the difference between the maximum τ_b, which occurs around θ = 0°, and the minimum τ_b, which occurs around θ = 180°, changes depending on the ϕ_2 value.

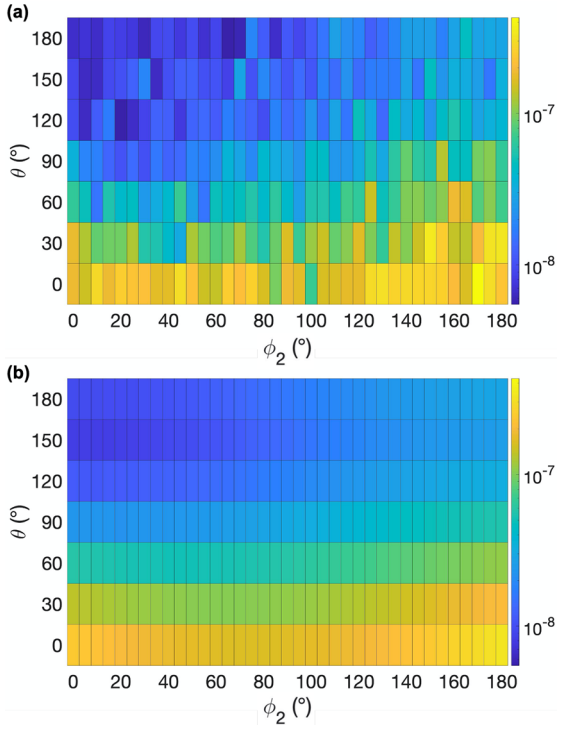

Figure 4. (a) Binding time as a function of θ and ϕ_2 with ϕ_1 = 180°. The time to bond, τ_b, for each θ−ϕ_2 pair is color coded according to a logarithmic scale. In the left section of the heatmap (0° ≤ ϕ_2 < 90°) the strands are in the trans configuration; for 90° < ϕ_2 ≤ 180°, the strands occupy the cis configuration. (b) Best fit for τ_b as a function of θ and ϕ_2 using the model in eq 3. In both heatmaps, the time to bond for each θ−ϕ_2 pair is color coded according to the same logarithmic scale.

https://doi.org/10.1021/acs.jpcb.1c00432
J. Phys. Chem. B 2021, 125, 4016−4024

In addition to recording τ_b, we also recorded the system configuration at intervals of 9.09×10^{-10} s. We used this data to determine which of the sticky-end base pairs had formed in the first time step with any sticky-end binding. In the majority of cases, multiple sticky-end base pairs formed before the first time step where sticky-end binding could be observed. This meant that the first observable instance of binding had multiple base pairs, making it impossible to determine precisely which base pair formed first. To display the dominant binding pathway for various ϕ_2–θ pairs, we considered the average initial base pair position $\overline{B}_0$, which we present in Figure 5.

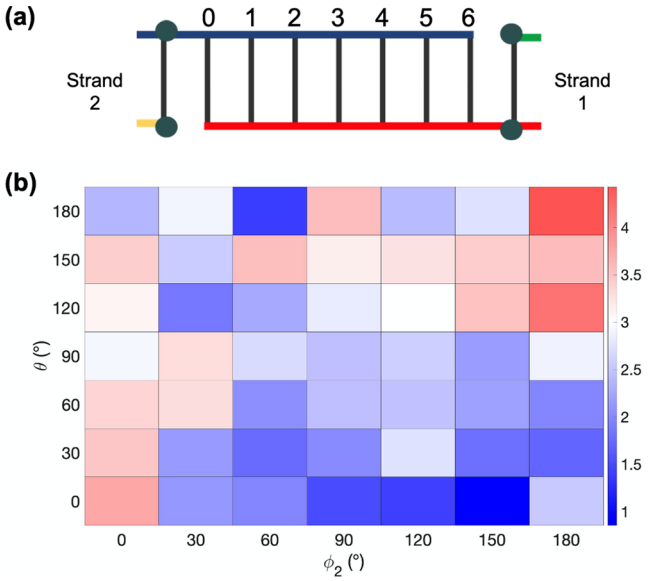

Figure 5. (a) Schematic showing the labeling scheme for the sticky-end base pairs. Base pair 0 is the base pair closest to strand 2, and base pair 6 is the base pair closes to strand 1. (b) Average initial base pair for various ϕ_2–θ pairs shown with a linear scale. A value of ~3 indicates no preference for initial hydrogen bond position. For each ϕ_2–θ pair, base pair data were collected from a total of eight runs with two SEICs, four runs from each SEIC. $\overline{B}_0 > 3$ are shown in shades of red; $\overline{B}_0 < 3$ are shown in shades of blue. Thus, red squares indicate a preference for forming initial base pairs closer to strand 1; blue squares indicate a preference for forming initial base pairs closer to strand 2. When $\overline{B}_0 = 3$ (white squares), initial base pairs form between all sticky-end nucleotides with equal probability.

When $\phi_2 > 60°$, the average initial base pair position $\overline{B}_0$ shifts from being closer to the attachment point on strand 2 ($\overline{B}_0 < 3$) to being closer to the attachment point on strand 1 ($\overline{B}_0 < 3$).

Figure 3 shows the binding time averages for each SEIC and the overall average for both $\phi_1 = 0°$ and $\phi_1 = 180°$. In both the $\phi_1 = 0°$ and $\phi_1 = 180°$ cases, plotting τ_b as a function of θ on a semilog plot reveals a sinusoidal curve with a minimum at $\theta \approx 140°$. For $\theta > 140°$, both curves are relatively flat. In this regime where the DNA strands are nearly antiparallel, further increasing the angle between the helical axes (θ) does not greatly impact the binding time. Note also that the $\overline{\tau}_b$ for $\phi_1 = 180°$ is globally less than $\overline{\tau}_b$ when $\phi_1 = 0°$. This indicates that binding between the sticky ends occurs more rapidly when the junction between the sticky ends and their corresponding dsDNA segments are on opposite sides of the plane containing the helical axes of both DNA strands (i.e., when the strands are in the trans configuration).

To further investigate the angular dependence of sticky-end binding, we characterize the binding interaction as a function of ϕ_2 (see Figure 1). In Figure 4 we plot the binding time, τ_b, as a function of θ and ϕ_2 with ϕ_1 held constant at 180°. The difference between ϕ_1 and ϕ_2 represents the relative azimuthal angle between the two strands. In Figure 4, for all θ values there is a clear increase in τ_b as ϕ_2 increases from 0° to 180°. When $\phi_2 < 90°$, the sticky ends are in the trans configuration, and when $\phi_2 > 90°$, the sticky ends are in the cis configuration. Therefore, this increase in τ_b indicates that binding between the sticky ends occurs more rapidly in the trans configuration than in the cis configuration, regardless of θ.

In Figure 6, we present the binding time τ_b for low, medium, and high temperatures (283, 310, and 363 K, respectively) for

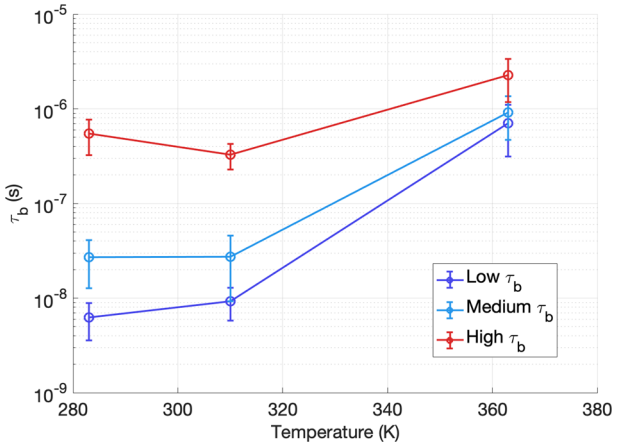

Figure 6. Binding time as a function of temperature for (θ, ϕ_1, ϕ_2) = (120°, 180°, 20°) (low τ_b), (θ, ϕ_1, ϕ_2) = (90°, 180°, 90°) (medium τ_b), and (θ, ϕ_1, ϕ_2) = (0°, 180°, 170°) (high τ_b). Binding time is shown on a logarithmic scale, and the three chosen temperature values (283, 310, and 363 K) are shown on a linear scale. For each point a 95% confidence interval is shown.

three angular configurations. The angular configurations chosen correspond to high, medium, and low values for τ_b as determined from previous simulations. With the exception of the high-τ_b configuration measured at high temperature, each point corresponds to a measurement of τ_b using ~20 SEICs each with four replicas. This specific number of SEICs (20) was chosen because it allowed for measurements of τ_b to be reasonably converged while remaining computationally tractable. For the high-τ_b configuration at high temperature, only a small number of runs yielded a binding time (see Figure 7). For the low- and medium-τ_b configurations there is a slight increase in binding time when moving from 283 to 310 K, although this increase is within the margin of error. For the high-τ_b configuration this trend reverses, and τ_b decreases when moving from 283 to 310 K. But for all configurations, the longest binding time was observed at 363 K.

Figure 7 shows the free energy profiles for three temperatures and angular configurations. Changing the angular configuration has a clear impact on the free energy curves, which indicates that the differences in the binding times observed at these three configurations is due in part to thermodynamic changes. Of particular note is the free energy profiles at high temperature (see Figure 7c). Changing the angular configuration of the strands at this temperature shifts the minimum of the free energy curve and changes the

https://doi.org/10.1021/acs.jpcb.1c00432
J. Phys. Chem. B 2021, 125, 4016−4024

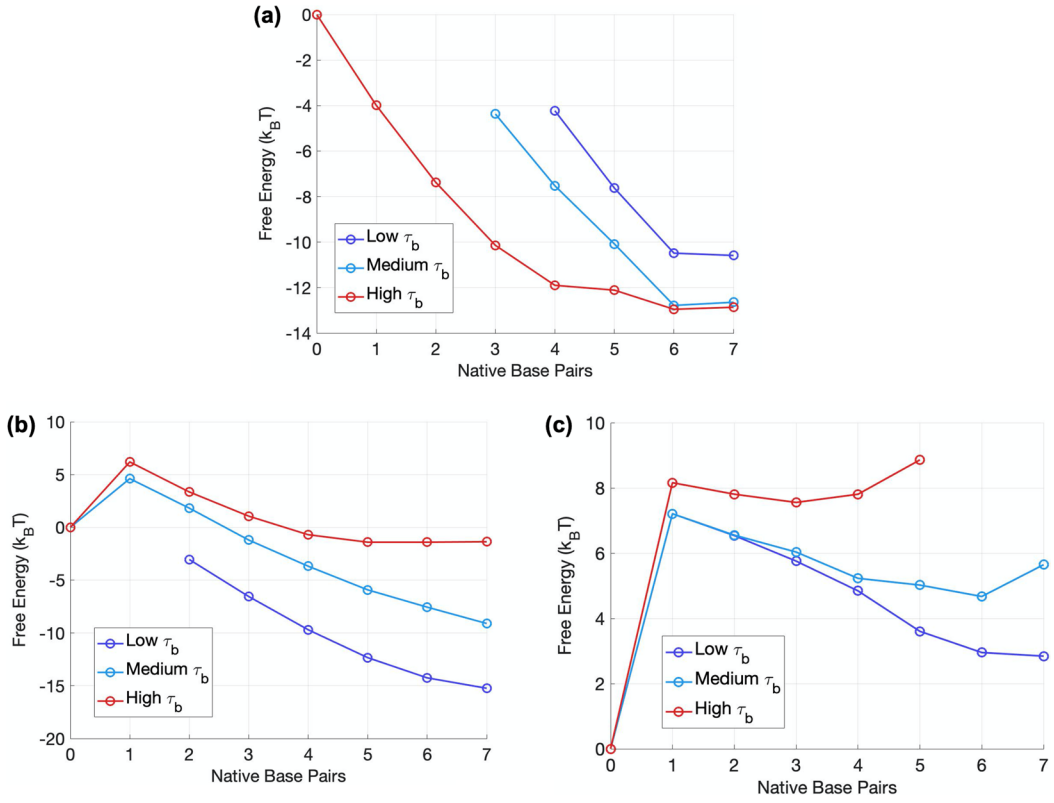

Figure 7. Free energy profiles for high-, medium-, and low-τ_b configurations. (a) Free energy profiles measured at low temperature (283 K). (b) Free energy profiles measured at medium temperature (310 K). (c) Free energy profiles measured at high temperature (363 K). Each free energy profile was constructed by using biased virtual move Monte Carlo (VMMC) simulations at the corresponding angular configuration. The zero for each free energy curve is set to the configuration with zero sticky-end base pairs. Gaps in the free energy profiles represent points with insufficient sampling of the reaction coordinate.

equilibrium number of sticky-end base pairs: in the low-τ_b configuration full sticky-end binding (seven sticky-end base pairs) is thermodynamically favorable, but in the high-τ_b configuration, three base pairs are thermodynamically favorable.

Trends in Binding Time τ_b. Next, we attempted to discern whether θ or ϕ_2 exerts the most control over τ_b. To do this, we will consider the ratio between the maximum and minimum τ_b within a given θ and ϕ_2:

$$R(\theta') = \frac{\max\{\tau_b(\theta = \theta', \phi_1 = 180^\circ, \phi_2)\}}{\min\{\tau_b(\theta = \theta', \phi_1 = 180^\circ, \phi_2)\}} \quad (1)$$

$$S(\phi_2') = \frac{\max\{\tau_b(\theta, \phi_1 = 180^\circ, \phi_2 = \phi_2')\}}{\min\{\tau_b(\theta, \phi_1 = 180^\circ, \phi_2 = \phi_2')\}} \quad (2)$$

$R(\theta')$ is the ratio between the maximum and minimum τ_b values that occur with $\theta = \theta'$; it measures the degree to which changing ϕ_2 influences τ_b. $S(\phi_2')$ is the ratio between the maximum and minimum τ_b values that occur with $\phi_2 = \phi_2'$; it measures the degree to which changing θ influences τ_b. We find that averaged over all θ values, $R \approx 10$, and when averaged over all ϕ_2 values, $S \approx 20$. This indicates that θ has a greater effect on τ_b than ϕ_2. The dependence on ϕ_2 is roughly constant across each theta value, with R never deviating far from the average of 9.8 ± 2.5. This is not the case for τ_b's dependence on θ. When $\Delta\phi < 90^\circ$, the maximum and minimum τ_b differ a factor of ∼10; when $\Delta\phi > 90^\circ$, the θ dependence is stronger, with maximum and minimum τ_b separated by a factor of ∼30. The transition between these two regimes for S occurs at ϕ_2 = 90°, reflecting the transition between the cis and trans configurations. In other words, when the strands are in the cis configuration, θ has less influence on the binding time than it does when the strands are in the trans configuration.

On the basis of our simulation results, we present a simple equation that phenomenologically describes the angular dependence of the sticky-end annealing time:

$$\tau_b(\phi_2, \theta) = \exp[C + A\cos(\phi_2 - \delta) + B\cos(\theta - \epsilon) + E\sin(\phi_2 - \delta)\cos(\theta - \epsilon)] \quad (3)$$

The parameter values that produce the best fit are A = −0.4453, B = 1.554, C = −16.5, E = −0.3446, δ = 38.68°, and ϵ = −25.26°. The primary trends of increase in τ_b as ϕ_2 increases and decrease in τ_b as θ increases are included in the model through the A and B terms, respectively. B is larger than A, indicating that the θ-dependence is stronger than the ϕ_2-dependence. These basic trends are altered by the cross-term associated with E and the two phase shift parameters δ and ϵ. One effect of these terms is to alter the position of the minimum τ_b for $\phi_2 < 90^\circ$ to $\theta = 150^\circ$. This shifted minimum matches the data well, as τ_b is slightly less at $\theta = 150^\circ$ compared to $\theta = 180^\circ$ when $\phi_2 < 90^\circ$. In addition, the model also contains intermediate minima between $\phi_2 = 0^\circ$ and $\phi_2 = 180^\circ$ within a given θ. These features are also present in the data as well, although at slightly different ϕ_2. In both cases, we speculate that the minima are the result of the changing distance between the attachment points as a function of θ and ϕ_2 and, therefore, that the annealing reaction between the

https://doi.org/10.1021/acs.jpcb.1c00432
J. Phys. Chem. B 2021, 125, 4016−4024

sticky ends is a function of this distance as well as the orientation between the dsDNA strands.

DISCUSSION

Factors Impacting Sticky-End Rigidity. We suspect that the observed angular dependence present in sticky-end binding primarily results from stacking interactions between adjacent bases of sticky ends. Compared to dsDNA, the persistence length of ssDNA is small. Accordingly, when considering a system composed of ssDNA and dsDNA segments, the ssDNA segments are often assumed to be very flexible.[42] Such an assumption would be valid for sticky ends markedly longer than the persistence length of ssDNA. But in the case of sticky ends as short as 10 nucleotides used in this study, the semiflexible nature of ssDNA must be considered.[43−47] Stacking between the first base of ssDNA and the end base pair of dsDNA also further restricts the orientational freedom of the sticky ends. A model that ignores this intrinsic rigidity would lead one to assume that the contortions required to achieve sticky-end binding are not thermodynamically unfavorable and, therefore, that sticky-end binding is largely independent of the angular orientation of the dsDNA segments. An individual segment of ssDNA is, however, known to have a nonzero persistence length, typically on the order of 6−12 Å.[45,48] Therefore, sticky ends, being ssDNA segments, possess intrinsic rigidity, which causes the binding reaction to be dependent on the mutual orientation between the sticky ends.

Adding to the rigidity of the sticky ends is the nearest-neighbor stacking interaction, which occurs between the first nucleotide of the sticky ends and the final base pair of the dsDNA segment. Stacking interactions are well-known to occur between adjacent base pairs in dsDNA segments.[49−51] These interactions also increase the thermodynamic stability of overhanging single-stranded segments via stacking between the terminal base pair and the first nucleotide of the overhang.[52] This interaction is a differentiating factor between ssDNA strands freely diffusing in solution and sticky ends. Therefore, ssDNA as an overhang to dsDNA is effectively stiffer than ssDNA with free ends. This difference in the boundary condition is borne out by previous measurements of the persistence length of ssDNA. The persistence length of an overhang ssDNA[53] is significantly larger than that of a freely diffusing ssDNA.[22,48]

In this study, we used a generic coarse-grained model and did not account for sequence-dependent stacking interactions. However, experimental studies[54] and sequence-dependent models[22] both show that poly dA has a longer persistence length than poly dT due to stronger helical stacking. In addition, computational studies have elucidated sequence-dependent effects in the formation of DNA minicircles.[55] However, it is not obvious how sequence dependence would affect the annealing rate because of the complementarity of sticky ends; increasing the rigidity of one sticky end will necessarily decrease the rigidity of the other sticky end. Therefore, we expect the binding time to change non-monotonically as one sticky-end sequence is varied from low to high purine content.

As shown in Figure 6, τ_b depends on temperature in a nontrivial manner. For the high-τ_b configuration, increasing the temperature from 283 to 310 K reduces the average binding time. Conversely, for the low-τ_b configuration, increasing temperature from 283 to 310 K increases the average binding time. We attribute these dependencies to the decrease in the persistence lengths of the ssDNA overhangs. For angular configurations that are unfavorable to binding (i.e., the high-τ_b configuration), this reduction in persistence length enables the sticky ends to twist and bend more easily, allowing them to bind with greater efficiency. For angular configurations that are favorable to binding (i.e., the low-τ_b configuration), however, a decrease in the persistence length allows the sticky ends to more freely deviate away from the favorable binding configuration established by the geometry, increasing the binding time. As the temperature is further increased from 310 to 363 K, the binding rate is no longer limited by the conformational fluctuations of the sticky ends, but instead governed by the enthalpic barrier of the transition state ($\Delta H^{\ddagger}$). Since $\Delta H^{\ddagger}$ is negative for base-pair formation, the binding rate would decrease with temperature ($\sim e^{-\Delta H^{\ddagger}/RT}$). This heuristic explanation is consistent with our result that τ_b for all configurations increases and converges when the temperature is changed from moderate (310 K) to high (363 K).

Dominant Pathway Analysis. Figure 5 shows the change in the average initial base pair $\bar{B}_0$ as a function of ϕ_2 and θ with $\phi_1 = 180°$. We made an interesting observation that the dominant binding pathway as determined by the average initial base pair changes as a function of the strand orientation. Specifically, for $\phi_2 > 60°$, $\bar{B}_0$ increases as θ increases from 0° to 180°. Because we did not employ the sequence-dependent capabilities of oxDNA2, this change cannot be a result of any sequence-dependent differences in persistence length between the two sticky ends. We speculate that this change in binding site preference is due to stacking interactions between the sticky-end nucleotides, which serve to bias the nucleotides toward facing inward toward the helical axis.[43−47] As ϕ_2 increases, the attachment point for the second sticky end moves counterclockwise. For $\phi_2 < 110°$, this decreases the distance between the attachment points and, in combination with stacking interactions, changes the preferred direction of the nucleotides. When $\phi_2 \approx 110°$, stacking interactions bias the nucleotides toward facing away from sticky end 1. For $\phi_2 > 110°$ the distance between the attachment points begins to increase, but the preferred direction of the sticky end 2 nucleotides becomes closer to horizontal. Therefore, $\phi_2 \approx 110°$ decreases the probability of sticky end 2 assuming a configuration that allows binding with sticky end 1. Meanwhile, the nucleotides of sticky end 1, pointing "horizontally" with $\phi_1 = 180°$, can bend toward sticky end 2 and bind with comparative ease and bind to their complementary nucleotide in sticky end 2. Thus, the sticky ends will prefer to bind closer to strand 2, and $\bar{B}_0$ is more likely to be <3. When $120° < \theta < 180°$, this effect is minimal, as much less bending is required to achieve binding since the strands are almost antiparallel. Therefore, one would expect no preference in the initial binding site in this regime, which is what the data show: in this regime, $\bar{B}_0$ randomly fluctuates around 3.

CONCLUSION

The oxDNA2 model is capable of simulating a system of 42 nucleotides on a microsecond time scale, which is sufficient to simulate rare events such as the breaking and forming of base pairs that occurs in sticky-end binding. In this study, we measured the time required for the sticky ends to transition from their initial configuration to the bound state by noting the time step at which the hydrogen binding energy dropped

https://doi.org/10.1021/acs.jpcb.1c00432
J. Phys. Chem. B 2021, 125, 4016−4024

below the critical value of −517.79 pN·nm, which indicated full binding between all the sticky-end nucleotides. The binding time τ_b was measured as a function of the angle between the helical axes of the dsDNA segments (θ), rotation around the helical axes for DNA segment 1 (ϕ_1), and rotation around the helical axis for DNA segment 2 (ϕ_2). Our simulations show that the binding rate between sticky ends is influenced by the orientation of the dsDNA segments they are attached to. Changing θ has a stronger effect on the binding rate than changing $\Delta\phi$. However, the degree to which θ influences the binding rate is modulated by $\Delta\phi$: when the DNA strands are in the cis conformation, the maximum and minimum τ_b differ by roughly a factor of 10; when the strands occupy the trans configuration, the θ dependence is stronger, with maximum and minimum τ_b separated by a factor of ∼30. Changing temperature, in addition to influencing the free energy, significantly impacts the binding rate possibly by reducing the rigidity of the sticky ends. The stand orientation also impacts the dominant binding pathway by changing the average initial binding site $\overline{B}_0$. These results are relevant for predicting hybridization efficiency of sticky ends that are rotationally restricted.

■ ASSOCIATED CONTENT

Supporting Information

The Supporting Information is available free of charge at https://pubs.acs.org/doi/10.1021/acs.jpcb.1c00432.

All initial conformations used for oxDNA simulations as well as other associated input files (ZIP)

■ AUTHOR INFORMATION

Corresponding Author

Harold D. Kim − *School of Physics, Georgia Institute of Technology, Atlanta, Georgia 30332, United States*; Email: harold.kim@physics.gatech.edu

Authors

Nicholas M. Gravina − *School of Physics, Georgia Institute of Technology, Atlanta, Georgia 30332, United States*

James C. Gumbart − *School of Physics, Georgia Institute of Technology, Atlanta, Georgia 30332, United States*; orcid.org/0000-0002-1510-7842

Complete contact information is available at: https://pubs.acs.org/10.1021/acs.jpcb.1c00432

Notes

The authors declare no competing financial interest.

■ ACKNOWLEDGMENTS

This work was supported by the National Science Foundation through the Division of Molecular and Cellular Biosciences (1517507) and the Physics of Living Systems Student Research Network (1806833). HDK also acknowledges support from the National Institutes of Health (R01GM112882). Computational resources were provided by the Partnership for an Advanced Computing Environment (PACE) at the Georgia Institute of Technology.

■ REFERENCES

(1) Vologodskii, A.; Frank-Kamenetskii, D. M. Strong bending of the DNA double helix. *Nucleic Acids Res.* **2013**, *41*, 6785−6792.

(2) Jeong, J.; Kim, H. D. Determinants of cyclization−decyclization kinetics of short DNA with sticky ends. *Nucleic Acids Res.* **2020**, *48*, 5147−5156.

(3) Zenk, J.; Tuntivate, C.; Schulman, R. Kinetics and thermodynamics of Watson−Crick base pairing driven DNA origami dimerization. *J. Am. Chem. Soc.* **2016**, *138*, 3346−3354.

(4) Yang, S.; Liu, W.; Wang, R. Control of the stepwise assembly−disassembly of DNA origami nanoclusters by pH stimuli-responsive DNA triplexes. *Nanoscale* **2019**, *11*, 18026−18030.

(5) Bartnik, K.; Barth, A.; Pilo-Pais, M.; Crevenna, A. H.; Liedl, T.; Lamb, D. C. A DNA Origami Platform for Single-Pair Förster Resonance Energy Transfer Investigation of DNA−DNA Interactions and Ligation. *J. Am. Chem. Soc.* **2020**, *142*, 815−825.

(6) Sheheade, B.; Liber, M.; Popov, M.; Berger, Y.; Khara, D. C.; Jopp, J.; Nir, E. Self-Assembly of DNA Origami Heterodimers in High Yields and Analysis of the Involved Mechanisms. *Small* **2019**, *15*, 1902979.

(7) Her, J.; Bunting, S. F. How cells ensure correct repair of DNA double-strand breaks. *J. Biol. Chem.* **2018**, *293*, 10502−10511.

(8) Pannunzio, N. R.; Watanabe, G.; Lieber, M. R. Nonhomologous DNA end-joining for repair of DNA double-strand breaks. *J. Biol. Chem.* **2018**, *293*, 10512−10523.

(9) Plunkett, C. E.; Lawley, S. D. Bimolecular binding rates for pairs of spherical molecules with small binding sites. *arXiv preprint arXiv:2002.11703* **2020**.

(10) Svozil, D.; Hobza, P.; Šponer, J. Comparison of intrinsic stacking energies of ten unique dinucleotide steps in A-RNA and B-DNA duplexes. Can we determine correct order of stability by quantum-chemical calculations? *J. Phys. Chem. B* **2010**, *114*, 1191−1203.

(11) Šponer, J.; Šponer, J. E.; Mládek, A.; Banáš, P.; Jurečka, P.; Otyepka, M. How to understand quantum chemical computations on DNA and RNA systems? A practical guide for non-specialists. *Methods* **2013**, *64*, 3−11.

(12) Mládek, A.; Krepl, M.; Svozil, D.; Čech, P.; Otyepka, M.; Banáš, P.; Zgarbová, M.; Jurečka, P.; Šponer, J. Benchmark quantum-chemical calculations on a complete set of rotameric families of the DNA sugar−phosphate backbone and their comparison with modern density functional theory. *Phys. Chem. Chem. Phys.* **2013**, *15*, 7295−7310.

(13) Laughton, C. A.; Harris, S. A. The atomistic simulation of DNA. *Wiley Interdiscip. Rev. Comput. Mol. Sci.* **2011**, *1*, 590−600.

(14) Pérez, A.; Luque, F. J.; Orozco, M. Frontiers in molecular dynamics simulations of DNA. *Acc. Chem. Res.* **2012**, *45*, 196−205.

(15) Zerze, G.; Stillinger, F.; Debenedetti, P. Thermodynamics of DNA Hybridization from Atomistic Simulations. *J. Phys. Chem. B* **2021**, *125*, 771.

(16) Waters, J. T.; Lu, X.-J.; Galindo-Murillo, R.; Gumbart, J. C.; Kim, H. D.; Cheatham, T. E.; Harvey, S. C. Transitions of Double-Stranded DNA Between the A- and B-Forms. *J. Phys. Chem. B* **2016**, *120*, 8449−8456.

(17) Waters, J. T.; Kim, H. D.; Gumbart, J. C.; Lu, X.-J.; Harvey, S. C. DNA Scrunching in the Packaging of Viral Genomes. *J. Phys. Chem. B* **2016**, *120*, 6200−6207.

(18) Yoo, J.; Li, C.-Y.; Slone, S. M.; Maffeo, C.; Aksimentiev, A. *DNA Nanotechnology*; Springer: 2018; pp 209−229.

(19) Lai, C.-L.; Chen, C.; Ou, S.-C.; Prentiss, M.; Pettitt, B. M. Interactions between identical DNA double helices. *Phys. Rev. E: Stat. Phys., Plasmas, Fluids, Relat. Interdiscip. Top.* **2020**, *101*, 032414.

(20) Snodin, B. E.; Randisi, F.; Mosayebi, M.; Šulc, P.; Schreck, J. S.; Romano, F.; Ouldridge, T. E.; Tsukanov, R.; Nir, E.; Louis, A. A.; et al. Introducing improved structural properties and salt dependence into a coarse-grained model of DNA. *J. Chem. Phys.* **2015**, *142*, 234901.

(21) Bustamante, C.; Marko, J.; Siggia, E.; Smith, S. Entropic elasticity of lambda-phage DNA. *Science* **1994**, *265*, 1599−1600.

(22) Chakraborty, D.; Hori, N.; Thirumalai, D. Sequence-dependent three interaction site model for single-and double-stranded DNA. *J. Chem. Theory Comput.* **2018**, *14*, 3763−3779.

(23) Matek, C.; Ouldridge, T. E.; Levy, A.; Doye, J. P.; Louis, A. A. DNA cruciform arms nucleate through a correlated but asynchronous cooperative mechanism. *J. Phys. Chem. B* **2012**, *116*, 11616−11625.
(24) Schmitt, T. J.; Rogers, J. B.; Knotts IV, T. A. Exploring the mechanisms of DNA hybridization on a surface. *J. Chem. Phys.* **2013**, *138*, 035102.
(25) Hinckley, D. M.; Lequieu, J. P.; de Pablo, J. J. Coarse-grained modeling of DNA oligomer hybridization: length, sequence, and salt effects. *J. Chem. Phys.* **2014**, *141*, 035102.
(26) Wang, Q.; Pettitt, B. M. Modeling DNA thermodynamics under torsional stress. *Biophys. J.* **2014**, *106*, 1182−1193.
(27) Romano, F.; Chakraborty, D.; Doye, J. P.; Ouldridge, T. E.; Louis, A. A. Coarse-grained simulations of DNA overstretching. *J. Chem. Phys.* **2013**, *138*, 085101.
(28) Prytkova, T. R.; Eryazici, I.; Stepp, B.; Nguyen, S.-B.; Schatz, G. C. DNA Melting in Small-Molecule-DNA-Hybrid Dimer Structures: Experimental Characterization and Coarse-Grained Molecular Dynamics Simulations. *J. Phys. Chem. B* **2010**, *114*, 2627−2634.
(29) Ouldridge, T. E.; Louis, A. A.; Doye, J. P. Structural, mechanical, and thermodynamic properties of a coarse-grained DNA model. *J. Chem. Phys.* **2011**, *134*, 085101.
(30) Ouldridge, T. E.; Louis, A. A.; Doye, J. P. DNA nanotweezers studied with a coarse-grained model of DNA. *Phys. Rev. Lett.* **2010**, *104*, 178101.
(31) Ouldridge, T. E.; Hoare, R. L.; Louis, A. A.; Doye, J. P.; Bath, J.; Turberfield, A. J. Optimizing DNA nanotechnology through coarse-grained modeling: a two-footed DNA walker. *ACS Nano* **2013**, *7*, 2479−2490.
(32) Rovigatti, L.; Smallenburg, F.; Romano, F.; Sciortino, F. Gels of DNA nanostars never crystallize. *ACS Nano* **2014**, *8*, 3567−3574.
(33) DeLuca, M.; Shi, Z.; Castro, C. E.; Arya, G. Dynamic DNA nanotechnology: toward functional nanoscale devices. *Nanoscale Horiz* **2020**, *5*, 182.
(34) Snodin, B. E.; Schreck, J. S.; Romano, F.; Louis, A. A.; Doye, J. P. Coarse-grained modelling of the structural properties of DNA origami. *Nucleic Acids Res.* **2019**, *47*, 1585−1597.
(35) Reshetnikov, R. V.; Stolyarova, A. V.; Zalevsky, A. O.; Panteleev, D. Y.; Pavlova, G. V.; Klinov, D. V.; Golovin, A. V.; Protopopova, A. D. A coarse-grained model for DNA origami. *Nucleic Acids Res.* **2018**, *46*, 1102−1112.
(36) Srinivas, N.; Ouldridge, T. E.; Šulc, P.; Schaeffer, J. M.; Yurke, B.; Louis, A. A.; Doye, J. P.; Winfree, E. On the biophysics and kinetics of toehold-mediated DNA strand displacement. *Nucleic Acids Res.* **2013**, *41*, 10641−10658.
(37) Mosayebi, M.; Romano, F.; Ouldridge, T. E.; Louis, A. A.; Doye, J. P. The role of loop stacking in the dynamics of DNA hairpin formation. *J. Phys. Chem. B* **2014**, *118*, 14326−14335.
(38) Machinek, R. R.; Ouldridge, T. E.; Haley, N. E.; Bath, J.; Turberfield, A. J. Programmable energy landscapes for kinetic control of DNA strand displacement. *Nat. Commun.* **2014**, *5*, 5324.
(39) Matek, C.; Ouldridge, T. E.; Doye, J. P.; Louis, A. A. Plectoneme tip bubbles: coupled denaturation and writhing in supercoiled DNA. *Sci. Rep.* **2015**, *5*, 7655.
(40) Stelzl, L. S.; Kells, A.; Rosta, E.; Hummer, G. Dynamic Histogram Analysis To Determine Free Energies and Rates from Biased Simulations. *J. Chem. Theory Comput.* **2017**, *13*, 6328−6342.
(41) Šulc, P.; Romano, F.; Ouldridge, T. E.; Rovigatti, L.; Doye, J. P. K.; Louis, A. A. Sequence-dependent thermodynamics of a coarse-grained DNA model. *J. Chem. Phys.* **2012**, *137*, 135101.
(42) Crothers, D. M.; Drak, J.; Kahn, J. D.; Levene, S. D. DNA bending, flexibility, and helical repeat by cyclization kinetics. *Methods Enzymol.* **1992**, *212*, 3−29.
(43) Tinland, B.; Pluen, A.; Sturm, J.; Weill, G. Persistence length of single-stranded DNA. *Macromolecules* **1997**, *30*, 5763−5765.
(44) Rechendorff, K.; Witz, G.; Adamcik, J.; Dietler, G. Persistence length and scaling properties of single-stranded DNA adsorbed on modified graphite. *J. Chem. Phys.* **2009**, *131*, 095103.
(45) Chi, Q.; Wang, G.; Jiang, J. The persistence length and length per base of single-stranded DNA obtained from fluorescence correlation spectroscopy measurements using mean field theory. *Phys. A* **2013**, *392*, 1072−1079.
(46) Kim, H. S.; Yingling, Y. G. Persistence Length of Single Stranded DNA: Effect of Length, Sequence and Surface. *Biophys. J.* **2014**, *106*, 278a.
(47) Roth, E.; Glick Azaria, A.; Girshevitz, O.; Bitler, A.; Garini, Y. Measuring the conformation and persistence length of single-stranded DNA using a DNA origami structure. *Nano Lett.* **2018**, *18*, 6703−6709.
(48) Chen, H.; Meisburger, S. P.; Pabit, S. A.; Sutton, J. L.; Webb, W. W.; Pollack, L. Ionic strength-dependent persistence lengths of single-stranded RNA and DNA. *Proc. Natl. Acad. Sci. U. S. A.* **2012**, *109*, 799−804.
(49) SantaLucia, J. A unified view of polymer, dumbbell, and oligonucleotide DNA nearest-neighbor thermodynamics. *Proc. Natl. Acad. Sci. U. S. A.* **1998**, *95*, 1460−1465.
(50) Zhang, T.-b.; Zhang, C.-l.; Dong, Z.-l.; Guan, Y.-f. Determination of base binding strength and base stacking interaction of DNA duplex using atomic force microscope. *Sci. Rep.* **2015**, *5*, 9143.
(51) Sattin, B. D.; Pelling, A. E.; Goh, M. C. DNA base pair resolution by single molecule force spectroscopy. *Nucleic Acids Res.* **2004**, *32*, 4876−4883.
(52) Bommarito, S.; Peyret, N.; Santa Lucia, J., Jr. Thermodynamic parameters for DNA sequences with dangling ends. *Nucleic Acids Res.* **2000**, *28*, 1929−1934.
(53) Murphy, M.; Rasnik, I.; Cheng, W.; Lohman, T. M.; Ha, T. Probing single-stranded DNA conformational flexibility using fluorescence spectroscopy. *Biophys. J.* **2004**, *86*, 2530−2537.
(54) Plumridge, A.; Meisburger, S. P.; Andresen, K.; Pollack, L. The impact of base stacking on the conformations and electrostatics of single-stranded DNA. *Nucleic Acids Res.* **2017**, *45*, 3932−3943.
(55) Wang, Q.; Pettitt, M. Sequence Affects the Cyclization of DNA Minicircles. *J. Phys. Chem. Lett.* **2016**, *7*, 1042−1046.

https://doi.org/10.1021/acs.jpcb.1c00432
J. Phys. Chem. B 2021, 125, 4016−4024